Phase Transitions in Tantalum-Modified Silver Niobate Ceramics for High Power Energy Storage

Ye Tian[1,2], Li Jin[1], Qingyuan Hu[1], Kun Yu[1], Yongyong Zhuang[1], Giuseppe Viola[3], Isaac Abrahams[4,5], Zhuo Xu[1], Xiaoyong Wei[1]*, Haixue Yan[2,5]*

[1]*Electronic Materials Research Laboratory, Key Laboratory of the Ministry of Education & International Center for Dielectric Research, School of Electronic and Information Engineering, Xi'an Jiaotong University, Xian 710049, China*

[2]*School of Engineering and Materials Science, Queen Mary University of London, Mile End Road, London E1 4NS, United Kingdom*

[3]*Department of Applied Science and Technology, Institute of Materials Physics and Engineering, Corso Duca degli Abruzzi 24, 10129 Torino, Italy*

[4]*School of Biological and Chemical Sciences, Queen Mary University of London, Mile End Road, London E1 4NS, United Kingdom*

[5]*Materials Research Institute, Queen Mary University of London, Mile End Road, London E1 4NS, United Kingdom*

Corresponding Authors*

wdy@xjtu.edu.cn and h.x.yan@qmul.ac.uk

Abstract

$Ag(Nb_{0.8}Ta_{0.2})O_3$ is used here as a model system to shed light on the nature of the low temperature phase behavior of the unsubstituted parent compound $AgNbO_3$, which is an important material for high-power energy storage applications. The three dielectric anomalies previously identified as $M_1 \leftrightarrow M_2$, T_f and $M_2 \leftrightarrow M_3$ transitions in $AgNbO_3$ ceramics are found to be intimately related to the polarization behavior of the B-site cations. In particular, the $M_1 \leftrightarrow M_2$ transition is found to involve the disappearance of original ferroelectric polar structure in the M_1 phase. Analysis of weak-field and strong field hysteresis loops in the M_2 region below T_f suggests the presence of a weakly-polar structure exhibiting antipolar behavior (i.e., a non-compensated antiferroelectric), which can be considered as ferrielectric (FIE). Modeling of the permittivity data using the Curie-Weiss law indicates that the Curie temperature is close to the freezing temperature T_f, which can be regarded as the Curie point of the FIE phase. Substitution by Ta^{5+} in this system enhances the stability of the weakly polar/antiferroelectric state giving rise to an increased energy storage density of 3.7 J cm^{-3} under an applied field of 27 MV m^{-1}, one of highest values ever reported for a dielectric ceramic. Furthermore, the energy storage capability remains approximately constant at around 3 J cm^{-3} up to 100 °C, at an applied field of 22 MV m^{-1}.

1. Introduction

Dielectric capacitors are employed as key components in numerous modern electronic devices. In particular, dielectric capacitors play an essential role in advanced energy storage and electrical power pulse electronic systems and related devices due to their ultrahigh power density and ultrafast charge and discharge speeds.[1] However, the development and large scale application of dielectric capacitors for high-power energy storage is limited by their relatively low values of energy storage density in the order of 1 J cm^{-3} for current commercial devices based on polypropylene thin films.[2] Therefore, the development of novel dielectric materials which overcome this energy storage limitation is seen as an essential step in meeting the demand from the increasingly growing market in microelectronic devices.[3,4] The energy storage density W in dielectric capacitors is governed by the ability of the dielectric material to separate static charges of opposite sign between two electrodes, which can be estimated as:

$$W = \int EdD \tag{1}$$

where D is the electric displacement and E is the external applied electric field.[5]

To realize high energy density, a dielectric material must simultaneously possess large electric displacement and high electric breakdown strength. In linear dielectrics, D is proportional to the external electric field, which is limited by the breakdown strength (E_b) of the dielectric. Generally, the permittivity of linear dielectrics is so small that it gives rise to low values of W, although they have high values of E_b, such as in the case of commercial polymer capacitors. Ferroelectrics (FEs) generally have much higher values of D, but most of the polarization is not released during electrical unloading, leading to low recoverable energy density. Antiferroelectrics (AFEs) are better candidates for realization of high energy density due to the reversible AFE $\leftrightarrow$ FE phase transitions that take place on application of an external electric field.[6,7] Pb-based antiferroelectric materials have been extensively studied for decades as energy storage devices.[8-10] However, environmental and health issues arising from the

use of lead-based materials have prompted ongoing research on suitable lead-free alternatives.[11-14]

Silver niobate ($AgNbO_3$) is a lead-free candidate for energy storage capacitors due to its large polarization (52 μC cm^{-2}) at high electric fields (220 kV cm^{-1}).[15] Structure investigations have confirmed that $AgNbO_3$ exhibits AFE behavior characterized by Ag^+ and Nb^{5+} antiparallel polarization.[16-18] However, early studies suggested that $AgNbO_3$ is in fact FE, with observed weak polarization hysteresis under a low applied field.[19-20] More recently, it was suggested that the observed weak polarization behavior could be explained by the presence of ferrielectric ordering.[21] We have shown that the coexistence of AFE and FE states leads to a complicated sequence of electric-field-induced events, which result in a high recoverable energy storage density of 2.1 J cm^{-3} for $AgNbO_3$ ceramics.[22] Compared to thin films, ceramics have larger effective volume for electrical energy storage, with the additional benefit of typically lower processing costs.[23-26]

In addition to the electric-field-induced polarization events, dielectric studies also reveal a series of dielectric anomalies related to a number of phase transitions, as described by the following sequence: [27-29]

$$M_1 \overset{\sim 70^\circ C}{\longleftrightarrow} M_2 \overset{\sim 170^\circ C}{\longleftrightarrow} T_f \overset{\sim 270^\circ C}{\longleftrightarrow} M_3 \overset{\sim 350^\circ C}{\longleftrightarrow} O \overset{\sim 380^\circ C}{\longleftrightarrow} T \overset{\sim 580^\circ C}{\longleftrightarrow} C.$$

The high temperature phases (above 350 °C) have been widely studied and confirmed, to correspond to orthorhombic (O) in space group *Cmcm* between 350 °C and 380 °C, tetragonal (T) in space group *P*4/*mbm* over the range 380 °C-580 °C and cubic (C) in space group *Pm*-3*m* at temperatures above 580 °C. Meanwhile, the nature of the three M phases is still under debate, although it is generally believed that they are related to the progressive evolution stages of Nb^{5+} dynamics.[18, 29] The T_f transition is considered to originate from a partial freezing of the Nb^{5+} displacements, which ultimately leads to an anti-polar configuration.[18, 29] A recent publication suggested that the $M_1 \leftrightarrow M_2$ transition involves a change in polarity, i.e. an FE ↔ AFE transition.[21]

The phase transitions and the polarization behavior of $AgNbO_3$ ceramics can be usefully tuned by compositional modification. In our previous study, Ag^+ was partially replaced by Bi^{3+} in the A-site which resulted in the progressive stabilization of long-range AFE order driven by a decrease of the perovskite tolerance factor due to the smaller ionic radius of Bi^{3+} compared to Ag^+.[30]

In the present work, we show that antiferroelectricity can also be conveniently enhanced by B-site substitution resulting in improved energy density in tantalum substituted $AgNbO_3$. It is known that silver tantalate ($AgTaO_3$) is an incipient ferroelectric/quantum paraelectric.[31] Recent research has shown that Ta^{5+} doping in $AgNbO_3$ results in reduced remnant polarization (P_r), enhanced field for the FE↔AFE transition and increased dielectric breakdown strength (E_b), which result in an enhanced energy storage density.[32] Early dielectric studies on the $AgNbO_3$-$AgTaO_3$ binary system revealed that the transitions between the M phases are highly sensitive to Ta^{5+} concentration.[33, 34] Other work has shown that at a concentration of 20 mol% Ta^{5+}, the $M_1 \leftrightarrow M_2$ transition shifts below room temperature.[35] Here we show that substitution of ferroelectrically active Nb^{5+} by non-ferroelectrically active Ta^{5+} in $AgNbO_3$ can minimize ferroelectric behaviour and enhance the AFE state, giving rise to improved energy storage density.

2. Experimental

Polycrystalline ceramic samples were synthesized by a conventional solid-state process using the standard mixed oxide route. Appropriate amounts of Ag_2O (99.7%), Nb_2O_5 (99.99%) and Ta_2O_5 (99.99%) to give a nominal formula of $Ag(Nb_{0.8}Ta_{0.2})O_3$ (ANT20) were ball-milled in ethanol for 12 h. After drying, the mixtures were placed in alumina boats and heated at a rate of 5 °C min^{-1} to 950 °C and calcined at this temperature for 4 h in flowing oxygen. The calcined powders were again ball-milled for 4 h in ethanol medium. After drying, the powders were mixed with 5 wt% polyvinyl alcohol (PVA) solution and pressed into pellets with a diameter of 15 mm and thickness of 1~2 mm under 500 MPa uniaxial pressure. After burning out the PVA

at 600 °C for 2 h, the samples were first sintered at 1090 °C for 6 h in flowing oxygen and then slow cooled to room temperature at a rate of -5 °C min^{-1}. The ceramic pellets were then re-sintered at 1100 °C for 6 h in flowing oxygen. The relative densities of the ceramics estimated by the Archimedes method were above 97%. The surface morphology of the thermally etched ceramic samples was observed using scanning electron microscopy (SEM) (Quanta FEG 250, FEI, USA) equipped with a backscattered electron detector. For crystal structural analysis, the sintered ceramic samples were crushed into fine powders which were then annealed at 500 °C for 20 min to remove residual stresses. X-ray powder diffraction data were collected on a PANalytical X'Pert Pro diffractometer (PANalytical, Cambridge, UK) fitted with an X'Celerator detector using Ni filtered Cu Kα radiation (λ = 1.5418 Å) over the range 5° to 120° 2θ, with a step width of 0.0167° and an effective count time of 400 s per step. The structural analysis was carried out by the Rietveld method using the GSAS software.[36] The starting models used for structure refinement were based on that of Levin *et al*.[18] in space group *Pbcm* and and Yashima *et al*.[21] in space group $Pb2_1m$ (transformed from $Pmc2_1$ in the original report). The temperature dependence of relative dielectric permittivity and dielectric loss at different frequencies were measured using an LCR meter (4284A, Agilent) with the sample placed in a tube furnace. The electrcic displacement-field (D-E) and current-field (I-E) hysteresis loops were measured using a ferroelectric analyzer (Aix ACCT TF 2000). The total energy storage density (W_{total}), recoverable/discharged energy storage (W_{rec}), energy loss density W_{loss} and energy efficiency η were calculated according to the following equations: [13]

$$W_{total} = \int_0^{D_{max}} EdD \quad (1)$$

$$W_{rec} = \int_{D_r}^{D_{max}} EdD \quad (2)$$

$$W_{loss} = W_{total} - W_{rec} \quad (3)$$

$$\eta = \frac{W_{rec}}{W_{total}} \times 100\% \quad (4)$$

3. Results and discussion

Figure 1 shows SEM images of the ANT20 ceramic. The average grain size is around 2.5 μm. No significant grain contrast could be spotted in back scattering mode as shown in Fig.1(b), suggesting that the ceramic is single phase. The true nature of the crystal structure of $AgNbO_3$ is still under debate. Early investigations using X-ray and neutron power diffraction methods confirmed that the structure could be well described by the non-polar *Pbcm* space group,[16-18] while a polar structure with space group $Pmc2_1$ (or $Pb2_1m$) has been proposed in more recent diffraction studies to explain electron diffraction images and weak ferroelectric behavior at low field.[21,22] In the present work, the structure refinement of ANT20 ceramic powders was carried out using both the non-polar *Pbcm* and polar $Pb2_1m$ models. The fitted diffraction patterns for these models are shown in Fig.2a and Fig.2b, respectively, with the refinement parameters listed in Table 1. All the observed diffraction peaks are well-fitted by both structural models, with similar reliability factors. Fig.2c shows the magnification of the XRD pattern in the range 10°-25° 2θ, with the positions of the allowed reflections indicated for both space groups. The absence of the (003) and (103) diffraction peaks unique to $Pb2_1m$ and the presence of (002), (100), (102) and (111) diffraction peaks common to both models, along with the slightly better fit reliability factors for the *Pbcm* model (R_{wp}= 0.0784, R_p=0.058 and χ^2=3.697) compared to those for the $Pb2_1m$ model (R_{wp}= 0.0818, R_p= 0.0616, and χ^2=4.033), suggest that the non-polar *Pbcm* model provides a better description of the crystallographic structure of ANT20.

Figure 3 shows the temperature-dependence of the relative dielectric constant (ε_r) and dielectric loss (tan δ) of ANT20, measured at different frequencies. As shown in Fig. 3a, a series of dielectric anomalies are observed in the relative permittivity plots. These can be attributed to particular transitions by direct comparison with those observed in $AgNbO_3$ (see above). [17,18,27,28] On heating, ε_r starts to increase above ~-100 °C, with a peak at ~ -25 °C, characterized by weak relaxor-like behavior, and attributable to the $M_1 \rightarrow M_2$ transition. On further heating, a broad peak with a

maximum around 170 °C corresponding to the $M_2 \rightarrow M_3$ transition is observed, while at higher temperature, a sharp peak occurs near 350 °C, attributable to the $M_3 \rightarrow O$ transition. The $O \rightarrow T$ transition seen in $AgNbO_3$ is less clear in the present case, but close inspection of the ε_r plot (Fig. 3a inset) shows a weak feature at ~375 °C, which likely corresponds to this transition. Within the M_2 phase region, another weak peak is evident at around 75 °C. A similar feature was observed in $AgNbO_3$ and attributed to the freezing temperature, T_f. The tan δ plot shown in Fig. 3b reveals three anomalies corresponding to the ε_r peaks at ~-25 °C, ~75 °C and ~350 °C. A summary of the observed transition temperatures in ANT20 ceramics is given in Table 2 along with those of pure $AgNbO_3$ for comparison. It can be noticed that the dielectric anomalies attributed to the $M_1 \leftrightarrow M_2$, T_f and $M_2 \leftrightarrow M_3$ transitions in ANT20 ceramics are significantly shifted to lower temperature compared to those in $AgNbO_3$ ceramics, while the dielectric anomalies related to $M_3 \leftrightarrow O$ and $O \leftrightarrow T$ phase transitions show negligible shifts.

There has been much discussion in the literature about the nature of the dielectric anomalies at ~70 °C, ~170 °C and ~270 °C in $AgNbO_3$.[17,18,28] Early studies suggested that the anomalies at ~70 °C and ~270 °C cannot be due to phase transitions between two different structures. Instead they were attributed to the progressive evolution stages of Nb^{5+} dynamics within the same average non-polar *Pbcm* structure.[17,18,28] In recent publications, the dielectric anomaly at ~70 °C has been suggested to be linked to a change of structure polarity (i.e., $Pbcm \leftrightarrow Pb2_1m$).[21,22] The dielectric anomaly at ~170 °C is commonly assigned to the freezing temperature (T_f), below which the antipolar Nb^{5+} ions displacements are frozen, resulting in antiferroelectric ordering.[18, 28] In the present system, where the B site cation Nb^{5+} is substituted for Ta^{5+} the observed shift in the three dielectric anomalies ($M_1 \leftrightarrow M_2$, T_f and $M_2 \leftrightarrow M_3$) suggests that they are intimately related to the polarization behavior of the B-site cation.

The Curie-Weiss law can used to describe thermodynamic phase transitions characterized by the formation of a spontaneous polarization (P_s) (e.g. FE phase transitions). It can also be used to describe AFE phase transitions which involve antiparallel polarization (i.e. antipolar) in subcells within a superlattice. [37,38] For AFE

↔ paraelectric (PE) or FE ↔ PE phase transitions, the non-linear dielectric behavior above the transition temperature should follow the Curie-Weiss law:

$$\frac{1}{\varepsilon_r} = \frac{T - T_0}{C} \quad (1)$$

where, C is the Curie-Weiss constant, T is the temperature and T_0 is the Curie temperature. For an ideal second order phase transition, $T_0 = T_C$, where T_C is the Curie point. Fig. 4 shows a fit using the Curie-Weiss law to the reciprocal of relative permittivity for the ANT20 ceramic. At higher temperatures (> 550 °C), the dielectric data contain contributions from conductivity, therefore only the data below 550 °C was used.in the fit. The fitted value of C is about 1.5×10^5. For the $M_3 \leftrightarrow O$ transition at around 380 °C, extrapolation of the $1/\varepsilon_r$ linear fit to zero gives a T_0 value of ~80 °C. In theory the system exhibits a thermally stable polar structure below T_0. It is interesting to note here that the value of T_0 seen in the ANT20 ceramic is close to T_f (75 °C).

Figure 5a shows the electric displacement-field (D-E) and current-field (I-E) hysteresis loops generated in two successive cycles for an ANT20 ceramic sample at room temperature, under an applied field of 6 MV m^{-1}. A tiny polarization hysteresis is observed in the D-E loop, with the I-E loop showing two current peaks. The remnant electric displacement is 1.3×10^{-3} C m^{-2}, which is half that found in $AgNbO_3$ ceramics under the same applied field,[26] suggesting that the structure of sample actually exhibits intrinsic weakly-polar (i.e. ferrielectric, FIE) characteristics, although the non-polar structure model provided a better description of the X-ray diffraction pattern. On initial loading, the current peak in the first quadrant can be attributed to the switching of ferrielectric domains in the virgin sample. On subsequent cycling, this peak becomes stronger, possibly due to the switching of additional field-induced polarization produced during cycling. At higher field (20 MV m^{-1}), double-like D-E loops with weak remnant polarization are observed (Fig.5b). The presence of current peaks at E_F and E_B (forward and backward fields) can be attributed to a reversible transition from the FIE state to an FE state induced at high

electric field. The persistence of weak current peaks near zero field, is consistent with presence of a thermally stable weakly-polar structure below T_f.

Fig. 6 shows the D-E and I-E hysteresis loops of an ANT20 ceramic, with successive cycles under a maximum applied field of 8 MV m^{-1} at different temperatures. It can be found that the polarization hysteresis progressively reduces and the current peaks (corresponding to polarization reversal event) become increasingly suppressed with increasing temperature approaching the $M_1 \leftrightarrow M_2$ transition temperature, until they completely disappear near T_f. To better visualize the evolution of the current peaks with temperature, the positive branch of the I-E curves at different temperatures are plotted in Fig.7. At -150 °C in the M_1 region, a sharp and symmetric current peak can be observed. The profile of the current peak becomes asymmetric at -60 °C and broadens at -30 °C. On approaching the $M_1 \leftrightarrow M_2$ transition temperature (~-25 °C), the peak narrows and decreases in intensity. These observations can be attributed to the overlapping of two current peaks, E_1 and E_2 as observed in $AgNbO_3$.[22] E_1 disappears near the $M_1 \leftrightarrow M_2$ transition (~-25 °C) and E_2 vanishes near the T_f transition (~75 °C). At -150 °C, the presence of symmetric current peaks (E_1), can be attributed to switching events involving the FE domains in the M_1 polar phase. On approaching the $M_1 \leftrightarrow M_2$ transition temperature, the polar FE domains reduce in size and a weakly-polar FIE phase begins to emerge, as evidenced by the coexistence of E_1 and E_2 current peaks. The observation of two polarization switching events at E_1 and E_2 is consistent with the coexistence of FE and FIE states in the M_1 region. In the M_2 region, the current peak E_1 disappears and the peak E_2 becomes symmetric again at room temperature, where it corresponds to switching of the weakly-polar FIE domains as discussed above. The disappearance of the E_2 current peak near T_f indicates that the FIE polar state vanishes.

Previously, T_f has been attributed to the freezing temperature of the antipolar dipoles, such that above T_f there is a random alignment of these dipoles.[22,29] Below T_f, the system is essentially antipolar, but can exhibit a very weak non-zero net polarization (i.e. FIE or non-compensated AFE) in nature. As mentioned above, the Curie temperature T_0 is very close to the observed value of T_f. This suggests that T_f

can be considered to be the Curie point (T_C) of the FIE phase. It is proposed that above T_f, the structure becomes AFE, consistent with the presence of linear D-E loops at low field (see Fig.6).

Figure 8 (a) compares the D-E hysteresis loops at 10 Hz of ANT20 and $AgNbO_3$ ceramics measured under maximum applied fields of 27 MV m^{-1} and 17.5 MV m^{-1}, respectively. For the ANT20 ceramic a typical double-like polarization hysteresis loop is observed, with weak remnant polarization and a field-induced ferroelectric polarization of 0.37 C m^{-2}. This value is slightly lower than that of $AgNbO_3$ ceramic (0.4 C m^{-2}), indicating that the introduction of tantalum also reduces the net field induced polarization. Moreover, the values of E_F and E_B also increase in the ANT20 ceramic compared to those for $AgNbO_3$, with respective E_F values of 17.5 MV m^{-1} and 12.5 MV m^{-1}, and E_B values of 12.5 MV m^{-1} and 5 MV m^{-1}. This reflects a higher stability of the antipolar state in ANT20 compared to $AgNbO_3$. The energy efficiency is inversely related to the difference between the transition fields ($\Delta E = E_F - E_B$). For ANT20 ceramic ΔE = is 5 MV m^{-1}, which compares to a value of 7.5 MV m^{-1} for $AgNbO_3$ ceramic. The higher transition fields and the smaller ΔE in ANT20 ceramic lead to a larger recoverable energy density (W_{rec}) as shown by the shaded areas in Fig.8a. Fig.8b shows D-E loops for an ANT20 ceramic sample under an applied field of 22 MV m^{-1} at different temperatures. The field-induced ferroelectric polarization decreases on heating, while the transition fields increase with increasing temperature. At 100 °C which lies above T_f, there is still a clear double-like D-E loop, related to AFE $\leftrightarrow$ FE transformation, while at 125 °C, the D-E loop is almost linear, indicating that there is only a limited degree of field-induced polarization.

Figure 9 shows the energy storage properties of ANT20 ceramic at different fields and temperatures. As shown in Fig. 9 (a), with increasing applied field, recoverable energy storage density (W_{rec}) increased. The maximum value for W_{rec} was 3.7 J cm^{-3} under an applied field of 27 MV m^{-1}. This value is significantly higher than the corresponding value for unsubstituted $AgNbO_3$ ceramics (2.1 J cm^{-3}).[22] Moreover, under an applied field of 22 MV m^{-1}, the ceramic maintains a high value for W_{rec} (~3 J cm^{-3}) which shows good thermal stability (± 6%) from room temperature up to 100 °C

(Fig. 9b). The energy efficiency, η, is higher than 70%. The recoverable energy storage density of the ANT20 ceramic is compared with that of other lead-free dielectric ceramics in Fig.10. It is evident that the ANT20 ceramic exhibits one of the highest recoverable energy storage density values of any known lead-free dielectric ceramic. Its W_{rec} value is comparable to the best $AgNbO_3$ and $K_{0.5}Na_{0.5}NbO_3$ based ceramics such as $Ag(Nb_{0.85}Ta_{0.15})O_3$ (ref. 32) and $0.9K0.5Na_{0.5}NbO_3$-$0.1Bi(Mg_{2/3}Nb_{1/3})O_3$ (ref. 13). Moreover, the high energy density of ANT20 is achieved at a relative low applied electrical field and generates a higher field induced polarization, which suggests great potential for application in high power energy storage capacitors.

4. Conclusions

20 mol% tantalum-modified $AgNbO_3$ single phase ceramics were successfully prepared using solid-state reaction followed by sintering in oxygen. The characteristic temperatures related to the $M_3 \leftrightarrow O$ (*Pbcm* ↔ *Cmcm*) and $O \leftrightarrow T$ (*Cmcm* ↔ *P*4/*mbm*) phase transitions did not show significant shifts from those in pure $AgNbO_3$, while those corresponding to $M_1 \leftrightarrow M_2$, T_f and $M_2 \leftrightarrow M_3$ transitions significantly shifted to lower temperature, indicating that these three dielectric anomalies are intimately related with the polarization behavior of the B-site cations. The observation of current peaks at E_1 and E_2 in the M_1 phase confirms the coexistence of polar FE and weakly-polar FIE states. The peak E_1 disappears in the M_2 region, while the peak E_2 vanishes above T_f. Modeling of the permittivity data using the Curie-Weiss law allows for extrapolation of the Curie point, which is found to be close to the freezing temperature T_f in this system. The structure of the M_2 phase below T_f is proposed to be ferrielectric, with a Curie point at T_f. The substitution of Nb^{5+} by Ta^{5+} on the B-site of $AgNbO_3$ enhances the stability of the weakly-polar/antipolar state and modifies the characteristic forward and backward fields, resulting in enhanced energy storage performance. A maximum of 3.7 J cm^{-3} recoverable energy storage density (W_{rec}) was achieved in ANT20 ceramic under an applied field of 27 MV m^{-1}, which represents

one of the highest values for any known lead-free ceramic. Moreover, the recoverable energy storage density is thermally stable, maintaining a value of around 3 J cm^{-3} up to 100 °C under an applied electric field cycle of 22 MV m^{-1}, making it of considerable interest for use in high-power energy storage.

Acknowledgements

This work was supported by the National Basic Research Program of China (Grant No. 2015CB654602), the International Science & Technology Cooperation Program of China (Grant No. 2015DFA51100), the NSFC projects (Grant Nos. 51761145024), Shaan Xi province projects (2015JM5199，2017 ktpt-21, 2018TD-024) and the 111 Project under Grant No. B14040.

References

1. B. Chu, X. Zhou, K. Ren, B. Neese, M. Lin, Q. Wang, F. Bauer, and Q. M. Zhang, *Science*, 2006, **313**, 334.
2. M. Rabuffi and G. Picci, *IEEE Trans. Plasma Sci.*, 2002, **30**, 1939.
3. Q. Li, L. Chen, M.R. Gadinski, S. Zhang, G. Zhang, H. Li, A. Haque, L. Chen, T. Jackson and Q.Wang, *Nature*, 2015, **523**, 576.
4. Z. Liu, T. Lu, J. Ye, G. Wang, X. Dong, R. Withers, and Y. Liu, *Adv. Mater. Technol*., 2018,1800111
5. Z. Dang, J. Yuan, S. Yao, and R. Liao, *Adv. Mater.*, 2013, **25**, 6334.
6. L. Jin, F. Li and S. Zhang, *J. Am. Ceram. Soc.*, 2014, **97**, 1.
7. X. Hao, J. Zhai, L. B. Kong and Z. Xu, *Prog. Mater. Sci.*, 2014, **63**, 1.
8. F. Li, J. Zhai, B. Shen, X. Liu, K. Yang, Y. Zhang, P. Li, B. Liu and H. Zeng, *J. Appl. Phys.*, 2017, **121**, 054103.
9. Y. Zhao, X. Hao and Q. Zhang, *ACS Appl. Mater. Interfaces*, 2014, **6**, 11633–11639.
10. B. Peng, Q. Zhang, X. Li, T. Sun, H. Fan, S. Ke, M. Ye, Y. Wang, W. Lu, H. Niu, X. Zeng,

and H. Huang, *ACS Appl. Mater. Interfaces*, 2015, **7**, 13512.

11. L. Jin, R. Huo, R. Guo, F. Li, D. Wang, Y. Tian, Q. Hu, X. Wei, Z. He, Y. Yan and G. Liu, *ACS Appl. Mater. Interfaces*, 2016, **8**, 31109–31119.
12. D. Damjanovic, N. Klein, L. Jin and V. Porokhonskyy, *Funct. Mater. Lett.*, 2010, **3**, 5–13.
13. T. Shao, H. Du, H. Ma, S. Qu, J. Wang, J. Wang, X. Wei, and Z. Xu, *J. Mater. Chem. A*, 2017, **5**, 554–563.
14. J. Wu, A. Mahajan, L. Riekehr, H. Zhang, B. Yang, N. Meng, Z. Zhang, and H. Yan, *Nano Energy*, 2018,**50,**723-732.
15. D. Fu, M. Endo, H. Taniguchi, T. Taniyama and M. Itoh, *Appl. Phys. Lett.*, 2007, **90**, 252907.
16. J. Fábry, Z. Zikmund, A. Kania and V. Petrícek, *Acta Crystallogr., Sect. C: Cryst. Struct. Commun.*, 2000, **56**, 916.
17. P. Sciau, A. Kania, B. Dkhil, E. Suard and A. Ratuszna, *J. Phys.: Condens. Matter*, 2004, **16**, 2795.
18. I. Levin, V. Krayzman, J. C. Woicik, J. Karapetrova, T. Proffen, M. G. Tucker and I. M. Reaney, *Phys. Rev. B*, 2009, **79**, 104113.
19. A. Kania, K. Roleder and M. Łukaszewski, *Ferroelectrics*, 1984, **52**, 265.
20. A. Kania and K. Roleder, *Ferroelectr., Lett. Sect.*, 1984, **2**, 51.
21. M. Yashima, S. Matsuyama, R. Sano, M. Itoh, K. Tsuda and D. Fu, *Chem. Mater.*, 2011, **23**, 1643.
22. Y. Tian, L. Jin, H. Zhang, Z. Xu, X. Wei, E. D. Politova, S. Y. Stefanovich, N. V. Tarakina, I. Abrahams and H. Yan, *J. Mater. Chem. A*, 2016, **4**, 17279–17287.
23. Z. Sun, C. Ma, M. Liu, J. Cui, L. Lu, J. Lu, X. Lou, L. Jin, H. Wang, and C. Jia, *Adv. Mater.* 2017, **29**, 1604427.
24. J. Li, F. Li, Z. Xu, and S. Zhang, *Adv. Mater.* 2018, 1802155
25. N. Kumar, A. Ionin, T. Ansell, S. Kwon, W. Hackenberger, D. Cann, *Appl. Phys. Lett.*, 2015, **106**, 252901.
26. D. Wang, Z. Fan, D. Zhou, A. Khesro, S. Murakami, A. Feteira, Q. Zhao, X. Tan, I. M. Reaney, *J. Mater. Chem. A*, **2018**, 6, 9
27. A. Kania and J. Kwapulínski, *J. Phys.: Condens. Matter*, 1999, **11**, 8933.
28. J. Gao, L. Zhao, Q. Liu, X. Wang, S. Zhang, and J. F. Li, *J. Am. Ceram. Soc.,* 2018, 1–8.

29. S. Miga, A. Kania, and J. Dec, *J. Phys.: Condens. Matter*, 2011, **23**, 155901.
30. Y. Tian, L. Jin, H. Zhang, Z. Xu, X. Wei, G. Viola, I. Abrahams, and H. Yan, *J. Mater. Chem. A*, 2017, **5**, 17525–17531.
31. H. P. Soon, H. Taniguchi, and M. Itoh, *Appl. Phys. Lett.*, 2009, **95**, 242904.
32. L. Zhao, Q. Liu, J. Gao, S. Zhang, and J. F. Li, *Adv. Mater.*, 2017, **29**, 1701824.
33. I. Levin, J. C. Woicik, A. Llobet, M. G. Tucker,V. Krayzman, J. Pokorny, and I. M. Reaney, *Chem. Mater.*, 2010, **22**, 4987–4995.
34. M. Valant, A.-K. Axelsson, and N. Alford, *J. Eur. Ceram. Soc.*, 2007, **27**, 2549–2560
35. H.U. Khan, K. Alam, M. Mateenullah, T. Blaschke, and B.S. Haq, *J. Eur. Ceram. Soc.*, 2015, **35**, 2775–2789.
36. A. C. Larson, R. B. Von Dreele, *Los Alamos National Laboratory Report*, 1987, No. LAUR-86-748.
37. C. Kittle, Phys. Rev., 1951, **82**,729-731.
38. M. J. Haun, T. J. Harvin, M. T. Lanagan, Z. Q. Zhuang, S. J. Jang, and L. E. Cross, J. Appl.Phys.,1989, **65**, 3173-3180.
39. Z. Shen, X. Wang, B. Luo and L. Li, *J. Mater. Chem. A*, 2015, **3**, 18146–18153.
40. L. Wu, X. Wang and L. Li, *RSC Adv.*, 2016, **6**, 14273.
41. T. Wang, L. Jin, C. Li, Q. Hu and X. Wei, *J. Am. Ceram. Soc.*, 2015, **98**, 559.
42. Q. Hu, L. Jin, T. Wang, C. Li, Z. Xing and X. Wei, *J. Alloys. Compd.*, 2015, **640**, 416.
43. W. Li, D. Zhou, L. Pang, R. Xu, and H. Guo, *J. Mater. Chem. A*, 2017, **5**, 19607–19612.
44. B. Qu, H. Du and Z. Yang, *J. Mater. Chem. C,* 2016, **4**, 1795.
45. Z. Yang, H. Du, S. Qu, Y. Hou, H. Ma, J. Wang, J. Wang, X. Wei, and Z. Xu, *J. Mater. Chem. A*, 2016, **4**, 13778–13785.
46. Y. H. Huang, Y. J. Wu, B. Liu, T. N. Yang, J. J. Wang, J. Li, L. Q. Chen, and X. M. Chen, *J. Mater. Chem. A*, 2018, **6**, 4477–4484.
47. B. Luo, X. Wang, E. Tian, H. Song, H. Wang, and L. Li, *ACS Appl. Mater. Interfaces*, 2017, **9**, 19963−19972.
48. H. Y. Zhou, X.Q. Liu, X.L. Zhu, X. M. Chen, *J. Am. Ceram. Soc*., 2018,**101**, 1999–2008.
49. H. Yang, F. Yan, Y. Lin, and T. Wang, *Appl. Phys. Lett.*, 2017, **111**, 253903.
50. H. Yang, F. Yan, Y. Lin, and T. Wang, *ACS Sustainable Chem. Eng*., 2017, **5**, 10215-10222.

51. H. Yang, F. Yan, Y. Lin, and T. Wang, *J. Alloys. Compd.*, 2017, **728**, 780-787.
52. H. Yang, F. Yan, Y. Lin, T. Wang, F. Wang, Y. Wang, L. Guo, W. Tai, and H. Wei, *J. Euro. Ceram. Soc*., 2017, **37**, 3303–3311.
53. Y. Pu, L. Zhang, Y. Cui, and M. Chen, *ACS Sustainable Chem. Eng.*, 2018, **6**, 6102–6109.
54. Q. Li, J. Wang, Y. Ma, L. Ma, G. Dong, and H. Fan, *J. Alloys. Compd.*, 2016, **663**, 701-707.
55. Q. Xu, M. T. Lanagan, X. Huang, J. Xie, L.Zhang, H. Hao, and H. Liu, *Ceram. Int.*, 2016, **42**, 9728−9736.
56. L. Zhao, Q. Liu, S. Zhang, and J. F. Li, *J. Mater. Chem. C*., 2016, **4**, 8380–8384.
57. L. Zhao, J. Gao, Q. Liu, S. Zhang, and J. F. Li, *ACS Appl. Mater. Interfaces.* 2018, **10**, 819–826.

Table 1 Refinement parameters for $Ag(Nb_{0.8}Ta_{0.2})O_3$ ceramic at 25 °C using non-polar *Pbcm* and polar $Pb2_1m$ structural models.

Chemical formula	$Ag(Nb_{0.8}Ta_{0.2})O_3$	
Formula weight	266.38	
Crystal system	Orthorhombic	
Space group	*Pbcm*	$Pb2_1m$
Unit cell dimensions(Å)	a = 5.54476(9)	a = 5.54499(3)
	b = 5.59658(0)	b = 5.59698(3)
	c = 15.68885(3)	c = 15.68960(9)
volume($Å^3$)	486.852	486.931
Z	8	8
Density(calculated)(g/cm^3)	7.268	7.267
R-factors	R_{wp} = 0.0784	R_{wp} =0.0818
	R_p = 0.0580	R_p = 0.0617
	R_{exp} = 0.0409	R_{exp} = 0.0409
	R_F^2 = 0.1020	R_F^2 = 0.0827
Total No. of variables	37	53
No. of profile points used	6880	6880

Table 2 Approximate polymorphic transition temperatures (°C) in $AgNbO_3$ and $Ag(Nb_{0.8}Ta_{0.2})O_3$ ceramics.

Polymorphic transitions	$AgNbO_3$	ANT20
$M_1 \leftrightarrow M_2$	70	-25
T_f	170	75
$M_2 \leftrightarrow M_3$	270	170
Pbcm ↔ *Cmcm*	350	350
Cmcm ↔ *P*4/*mbm*	380	375

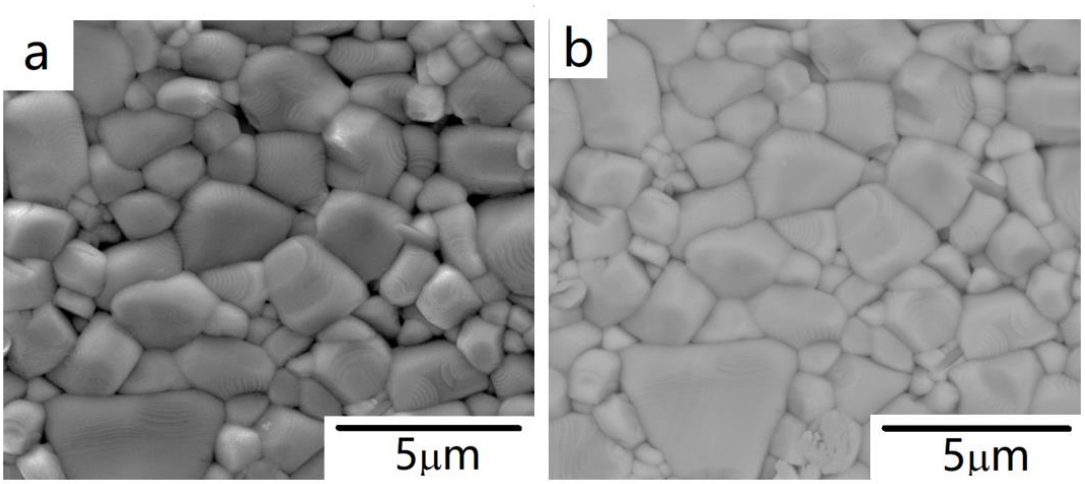

Fig. 1. SEM micrographs of the surface of an ANT20 ceramic showing (a) secondary electrons image and (b) backscattered electron image.

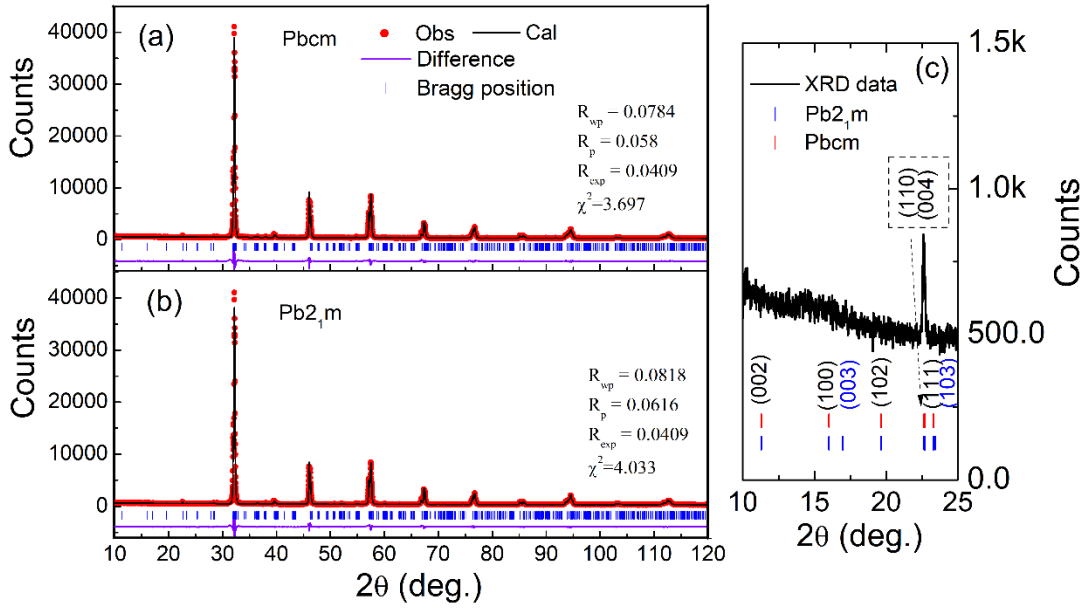

Fig. 2. Fitted X-ray powder diffraction (XRD) pattern of ANT20 ceramic powders using (a) *Pbcm* model and (b) *Pb*2₁*m* model; (c) observed XRD data at low angles with reflection positions for *the Pbcm* and *Pb*2₁*m* models indicated.

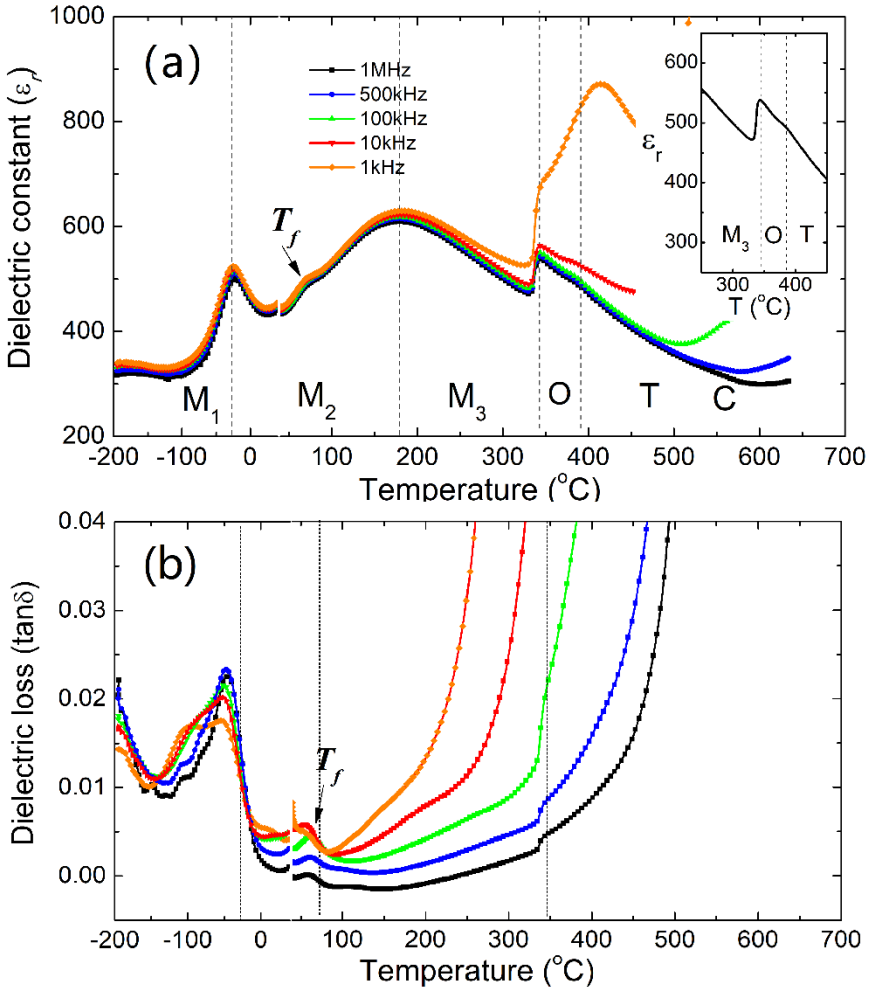

Fig.3. Temperature-dependence of (a) relative permittivity (ε_r, with detail of the O ↔ T transition at 1 MHz inset) and (b) dielectric loss (tan δ) for ANT20 ceramic.

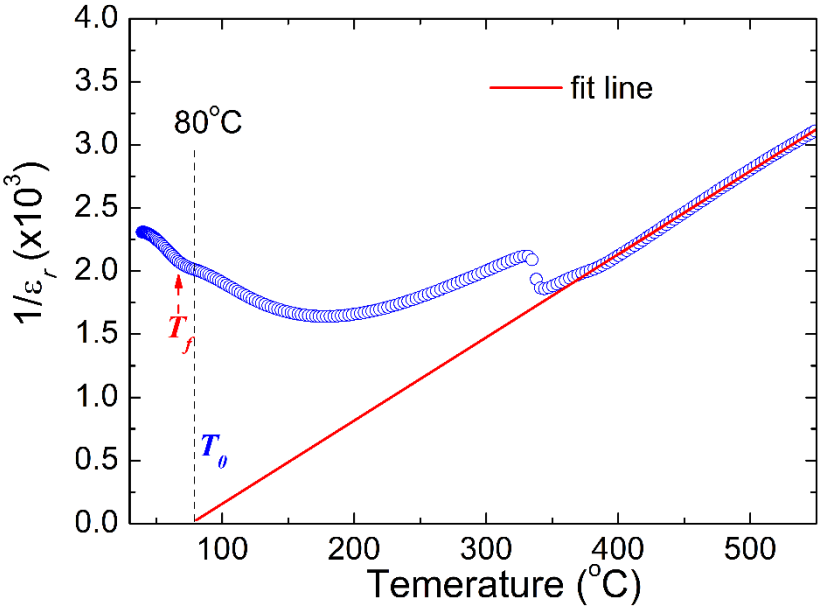

Fig. 4. Temperature-dependence of reciprocal relative permittivity ($1/\varepsilon_r$) for ANT20 ceramic measured at 1 MHz

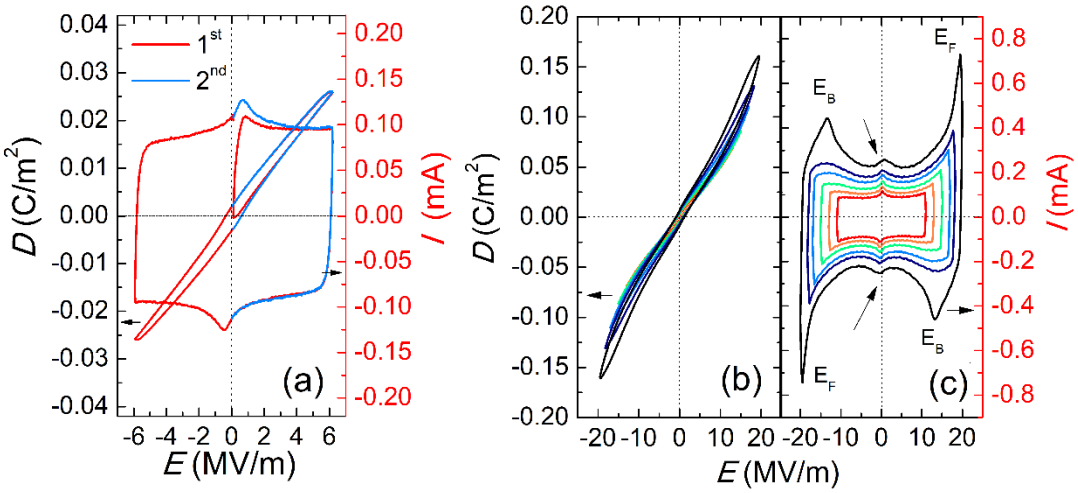

Fig. 5. Dielectric displacement-field (D-E) and current-field (I-E) hysteresis loops for ANT20 ceramic at 10 Hz: (a) under an applied field of 6 MV m^{-1} generated in the initial two cycles. (b) and (c) successive cycles under applied fields from 10 to 20 MV m^{-1}.

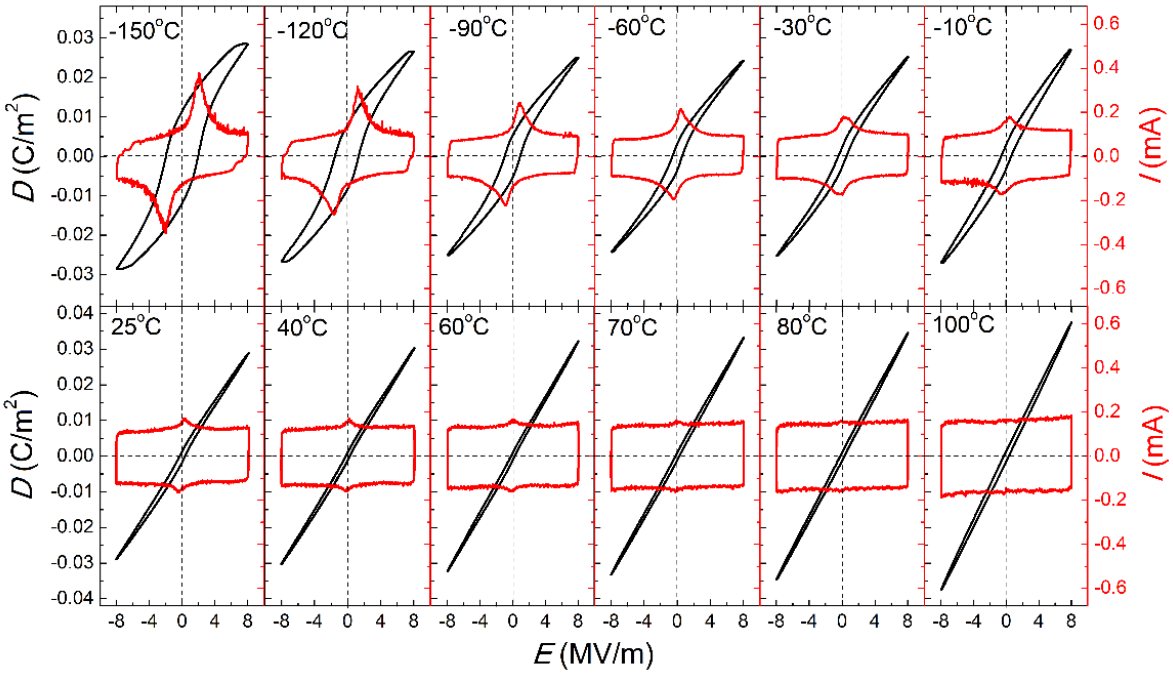

Fig. 6. Successively cycled D-E and I-E hysteresis loops at 10 Hz for ANT20 ceramic under an applied field of 8 MV m^{-1} at different temperatures.

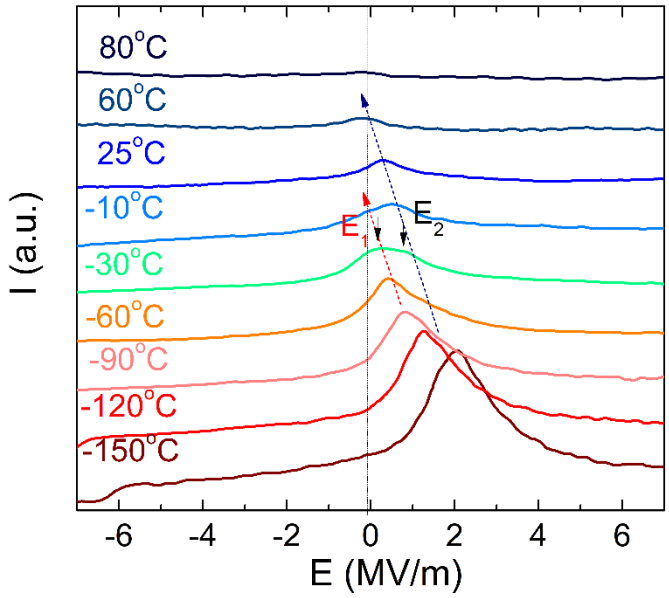

Fig. 7. Detail of the I-E curves for ANT20 ceramic at 10 Hz under an applied field of 8 MV m^{-1} at different temperatures.

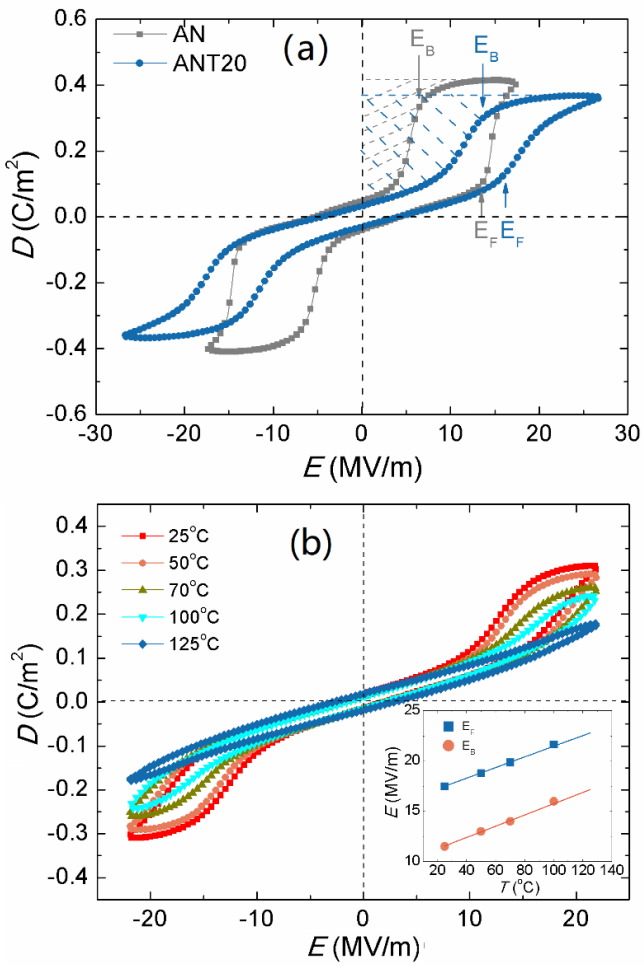

Fig.8 (a) D-E hysteresis loops for ANT20 and $AgNbO_3$ ceramics measured at maximum applied fields of 27 and 17.5 MV m^{-1}, respectively. The shaded areas represent the recoverable energy storage density; (b) D-E hysteresis loops for ANT20 ceramic at different temperatures on heating. The thermal dependences of the forward and backward transition fields (E_F and E_B) generated from the *dD*/*dE* curves are shown in the inset.

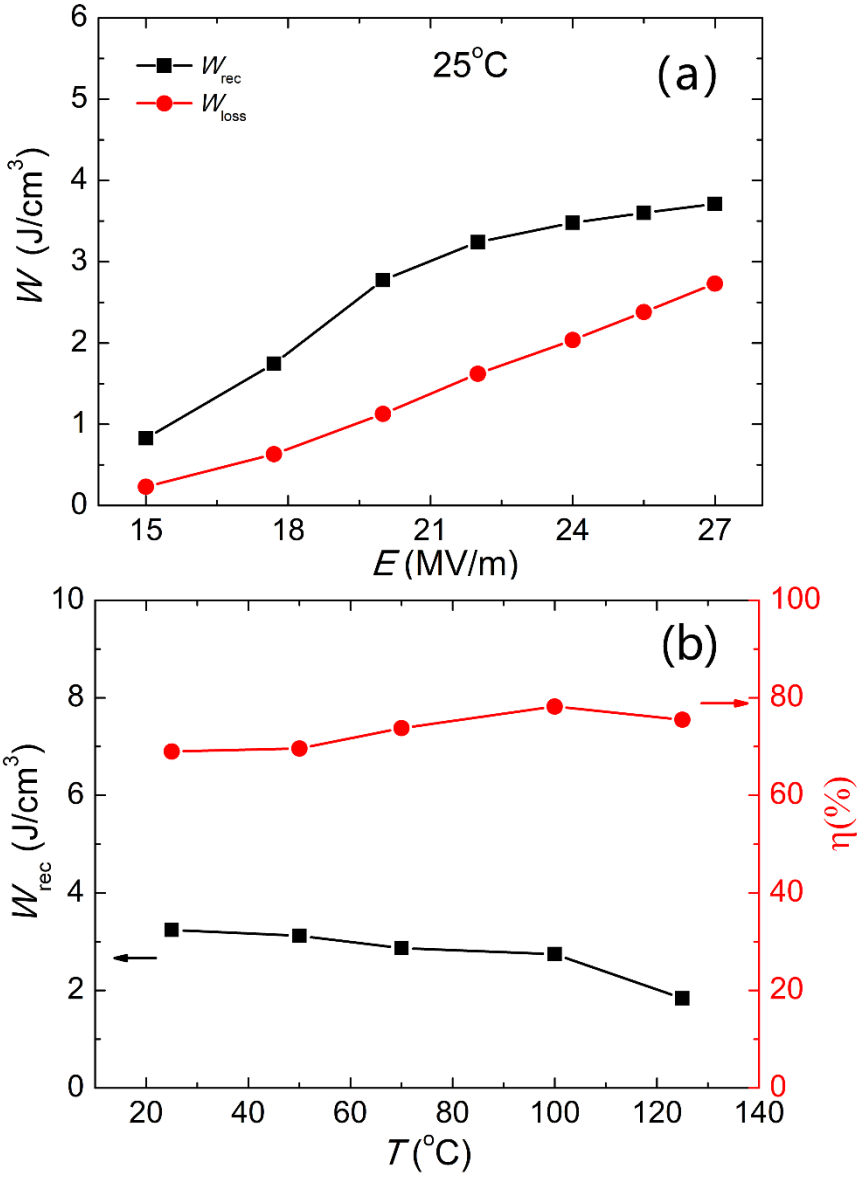

Fig.9. (a) Electric field variation of energy density (W_{rec}) in ANT20 ceramic and (b) thermal variation of energy density(W_{rec}) and energy efficiency (η) of ANT20 ceramic at an applied field of 22 MV m^{-1}.

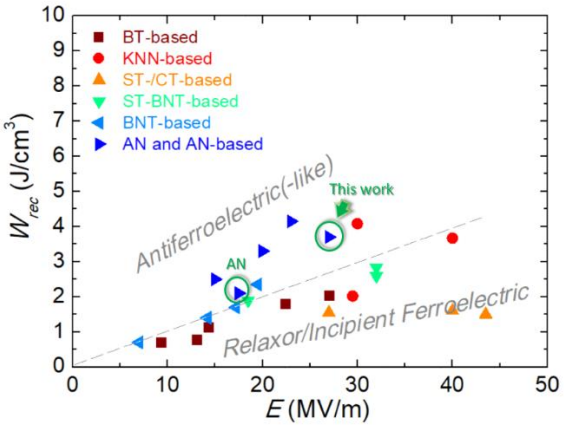

Fig.10. Comparison of recoverable energy density (W_{rec}) in ANT20 ceramic with that in other lead-free dielectric ceramic systems: $BaTiO_3$ (BT)-based[39-43]; $K_{0.5}Na_{0.5}NbO_3$ (KNN)-based[13,44,45]; $CaTiO_3$(CT)-based[46,47]; $SrTiO_3$(ST)-based[48]; $SrTiO_3$-$Ba_{0.5}Na_{0.5}TiO_3$ (ST-BNT)-based[49-51]; $Ba_{0.5}Na_{0.5}TiO_3$(BNT)-based[52-55]; $AgNbO_3$ (AN)-based[22,30, 32,56,57].